Supplementary Information - First-principles calculations to identify key native point defects in $Sr_4Al_{14}O_{25}$

William Lafargue-Dit-Hauret,[a] Camille Latouche,[a*] Mathieu Allix,[b] Bruno Viana,[c] and Stephane Jobic[a‡]

[a] *Université de Nantes, CNRS, Institut des Matériaux Jean Rouxel, IMN, F-44000 Nantes, France*

[b] *Conditions Extrêmes et Matériaux: Haute Température et Irradiation, CEMHTI, UPR 3079, CNRS, Université Orléans, Orléans 45071, France*

[c] *PSL Research University Chimie ParisTech, IRCP, CNRS, Paris, 75005 France*

[*] *E-mail: camille.latouche@cnrs-imn.fr*

[‡] *E-mail: stephane.jobic@cnrs-imn.fr*

I Corrections applied to defect formation enthalpies

Defect formation enthalpies (DFEs) were computed using the PyDEF package [1,2] which enables to properly take into account several post-treatment corrections needed in this study. Here, the following corrections were considered (detailed hereafter):

- Band-edges shift (BS)
- Perturbated Host State (PHS)
- Potential alignment (PA)
- Moss-Burstein (MB)
- Makov-Payne (MP)

Band-edges shift correction During our theoretical investigations, we used the meta-GGA SCAN functional to perform structural relaxations and determine accurate total energies. This method allows us to simulate lattice parameters in good agreement with experimental values, but we do not recover the experimental electronic band gap reported at 6.3 eV [3]. Unfortunately, this property is of particular importance to properly predict DFEs for point defects. We fixed this issue with a rigid shift of band-edges (*i.e.*, Valence Band Maximum and Conduction Band Minimum, respectively abbreviated by VBM and CBM) to fit with values obtained with a PBE0 functional calculation done on the fully relaxed SCAN structure. For a defect D of charge state q, the contribution of the band shift (BS) correction to DFEs is formulated as:

$$\Delta E_{BS} = q \times \Delta E_V \tag{1}$$

where ΔE_V corresponds to the shift in energies of the VBM between the SCAN and PBE0 functionals.

Perturbated Host State correction In contrast to point defects with deep electronic states, the shifting of VBM and CBM values by the BS correction may significantly affect DFEs for shallow defects. More specifically, when defect localized states are lying within the bottom of the conduction band (the top of the valence band), the electrons (holes) which occupy these states relaxed and tend to stabilize within a perturbated host state (PHS). The related contribution to DFEs expresses as

$$\Delta E_{PHS} = z_{e^-} \Delta E_C - z_{h^+} \Delta E_V \tag{2}$$

where ΔE_C is the shift of CBM, ΔE_V is the shift of VBM, z_{e^-} the number of free electrons within the conduction band and z_{h^+} the number of free holes within the valence band.

Potential Alignment correction When one introduces a net charge q into a neutral system, energy levels are shifted by an unknown quantity. In such a situation, the direct comparison with the bandstructure of the host system can be addressed with an alignment of the VBM for the charged system. The Potential Alignment (PA) correction is described by the following expression:

$$\Delta E_{PA} = q \times \overline{\Delta V} \tag{3}$$

where $\overline{\Delta V}$ corresponds to the average of the potential felt by atoms beyond a specific distance of the point defect.

Moss-Burstein correction Our computational strategy is based on the supercell approach for which point defects are considered sufficiently diluted into the matrix. If the size of the supercell is too small, a Moss-Burstein-like effect may be observed due to the presence of PHSs. Here, band-filling effects were removed for shallow states considering the Moss-Burstein (MB) term [4,5] formulated as:

$$\Delta E^{e^-}_{MB} = -\sum^{n,k} \omega_k \eta_{n,k} \left(\varepsilon_{n,k} - \left[E^{host}_C + \overline{\Delta V} \right] \right) \cdot \Theta \left(\varepsilon_{n,k} - \left[E^{host}_C + \overline{\Delta V} \right] \right) \tag{4}$$

and for the holes as:

$$\Delta E^{h^+}_{MB} = -\sum^{n,k} \omega_k \left(2 - \eta_{n,k}\right) \left(\left[E^{host}_V + \overline{\Delta V} \right] - \varepsilon_{n,k} \right) \cdot \Theta \left(\left[E^{host}_V + \overline{\Delta V} \right] - \varepsilon_{n,k} \right) \tag{5}$$

where ω_k is the weight of k-point k, $\eta_{n,k}$ is the occupation of band n for k-point k, $\varepsilon_{n,k}$ is the energy of band n for k-point k, and Θ is the Heaviside function.

Makov-Payne correction For periodic boundary approaches, the presence of charge point defects introduces spurious electrostatic interactions. In 2009, Lany and Zunger formulated a general scheme [6] to remove these effects:

$$\Delta E_{MP} = \left(1 + c_{sh}\left(1 - \varepsilon^{-1}\right)\right) \frac{q^2 \alpha_M}{2\varepsilon\Omega^{1/3}} \tag{6}$$

where c_{sh} is a geometry dependent correction term, ε is the dielectric constant of the material, α_M is the Madelung constant and Ω the volume. In our study, $c_{sh} = \frac{1}{3}$.

Despite the existence of many investigations, the experimental value for dielectric constant still remains unknown. On the theoretical side, the significant computational cost induces by the use of plane wave basis set does not allow to access this parameter. CRYSTAL17 calculations using the PBE0 functional were dedicated for this. We found $\varepsilon = 8.77$, close to data reported for the strontium aluminate compound $SrAl_2O_4$.

II Method for computing defect concentrations

To estimate the point defect concentrations, one may solve the charge neutrality equation formulated as:

$$-n_{e^-}(E_F)+n_{h^+}(E_F)+\sum_D\sum_{q_i\in q_D} q_i\cdot n_{D,q_i}(E_F)=0 \tag{7}$$

In Equation 7, n_{D,q_i} is the defect concentration for the defect D of charge q_i:

$$n_{D,q_i}\left(E_F^{gr}\right)\approx\frac{N}{\Omega}\cdot exp\left(-\frac{\Delta_f H^{D,q_i}\left(E_F^{gr}\right)}{k_B T_{gr}}\right) \tag{8}$$

where N is the number of sites, Ω the volume, k_B is the Boltzmann constant, and $\Delta_f H^{D,q_i}$ the defect formation enthalpy.
In Equation 7, n_{e^-} and n_{h^+} correspond to the free electrons and holes, respectively:

$$n_e(E_F)=\int_{E_C}^{+\infty} g_e(E)\,f_{FD}(E-E_F)\,dE \tag{9}$$

$$n_h(E_F)=\int_{-\infty}^{E_V} g_h(E)\,(1-f_{FD}(E-E_F))\,dE \tag{10}$$

where $f_{FD}(E-E_F)$ is the Fermi-Dirac function given as:

$$f_{FD}(E-E_F)=\frac{1}{1+exp\left(\frac{E-E_F}{k_B T}\right)} \tag{11}$$

and $g_i(E)$ the 3D density of states of holes and electrons:

$$g_{e,h}(E)=\frac{1}{4\pi^2}\left(\frac{2m^*_{e,h}}{\hbar^2}\right)^{\frac{3}{2}}\sqrt{E} \tag{12}$$

where m_e^* and m_h^* are the electron and hole effective masses (calculated for the ideal host lattice), respectively. These values were estimated based on the parabolic fitting function:

$$E(\boldsymbol{k})=\frac{\hbar}{2m^*}\boldsymbol{k}^2 \tag{13}$$

III Symmetry inequivalent sites

Site	Wyckoff	x_{th}	y_{th}	z_{th}	x_{exp}	y_{exp}	z_{exp}
Sr(1)	4*j*	0.1380	0.5000	0.0378	0.1376	0.5000	0.0330
Sr(2)	4*i*	0.1208	0.0000	0.1138	0.1208	0.0000	0.1130
Al(1)	8*l*	0.1855	0.1948	0.6298	0.1850	0.1980	0.6330
Al(2)	8*l*	0.0662	0.3219	0.5075	0.0664	0.3260	0.5100
Al(3)	4*k*	0.2500	0.2968	0.1350	0.2500	0.2990	0.1270
Al(4)	4*h*	0.0000	0.1676	0.0000	0.0000	0.1760	0.0000
Al(5)	2*a*	0.0000	0.0000	0.5000	0.0000	0.0000	0.5000
Al(6)	2*d*	0.0000	0.5000	0.0000	0.0000	0.5000	0.0000
O(1)	8*l*	0.0429	0.1593	0.3230	0.0422	0.1570	0.3280
O(2)	8*l*	0.1368	0.3228	0.5039	0.1368	0.3290	0.5020
O(3)	8*l*	0.1905	0.2290	0.9827	0.1908	0.2290	0.9820
O(4)	4*k*	0.2500	0.2306	0.4801	0.2500	0.2360	0.4730
O(5)	4*i*	0.0388	0.0000	0.8284	0.0391	0.0000	0.8230
O(6)	4*j*	0.0497	0.5000	0.3269	0.0507	0.5000	0.3230
O(7)	4*i*	0.1658	0.0000	0.5831	0.1651	0.0000	0.5740
O(8)	8*l*	0.0427	0.3372	0.8479	0.0444	0.3440	0.8420
O(9)	2*f*	0.2500	0.5000	0.1208	0.2500	0.5000	0.0970

Table S1 Comparison of the reduced coordinates for irreducible crystallographic sites in experimental and SCAN structures.

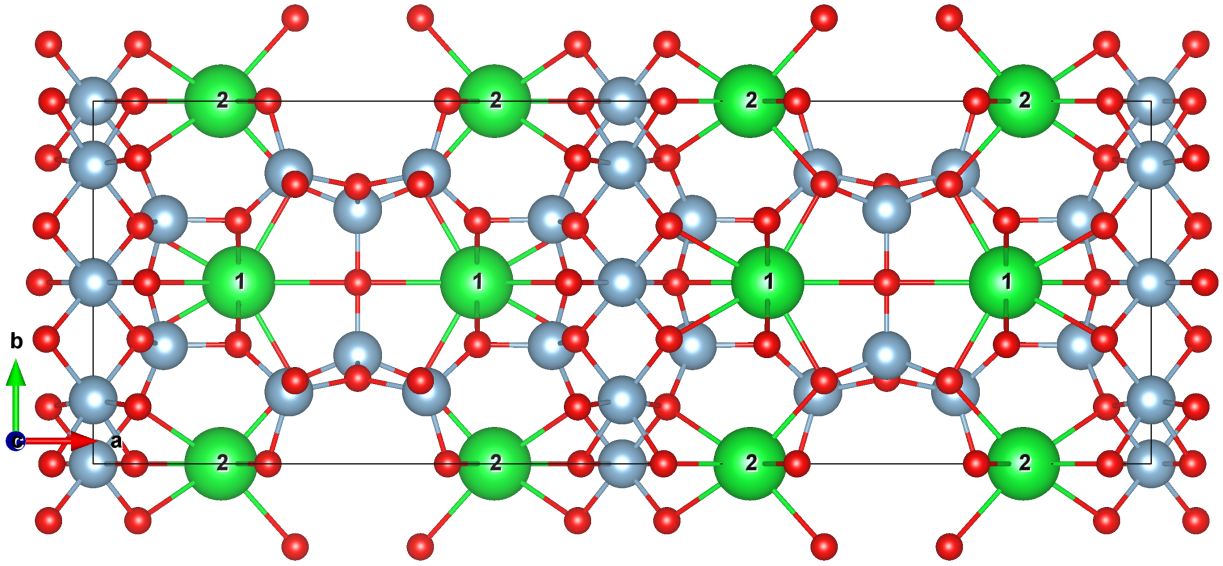

Fig. S1 Symmetrically non-equivalent Sr sites. Strontium, aluminium and oxygen atoms are represented by green, blue and red spheres, respectively.

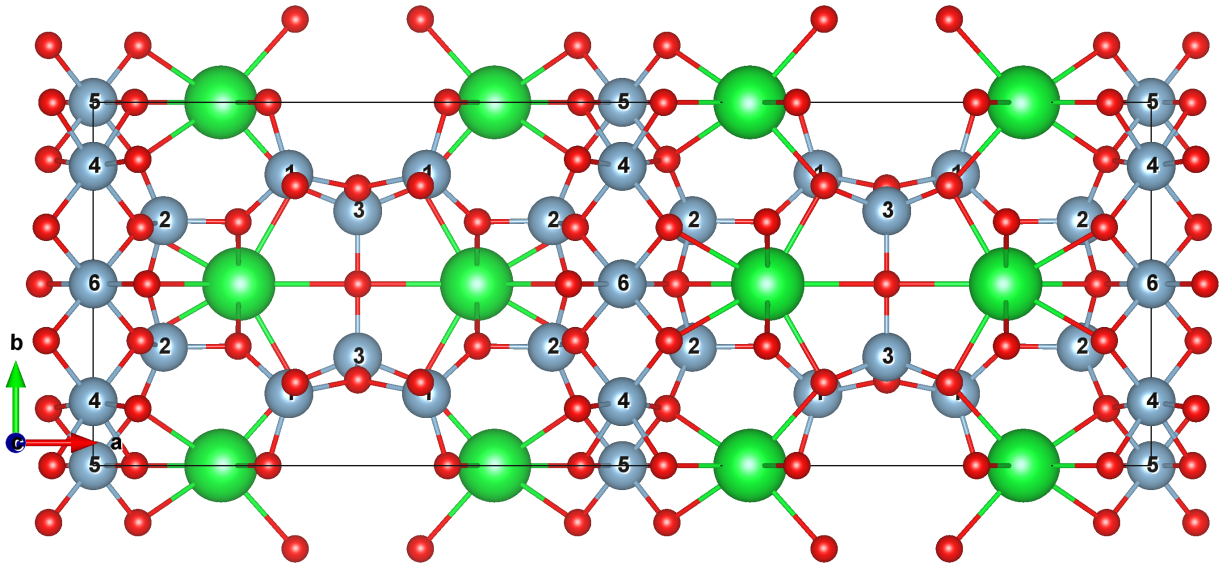

Fig. S2 Symmetrically non-equivalent Al sites. Strontium, aluminium and oxygen atoms are represented by green, blue and red spheres, respectively.

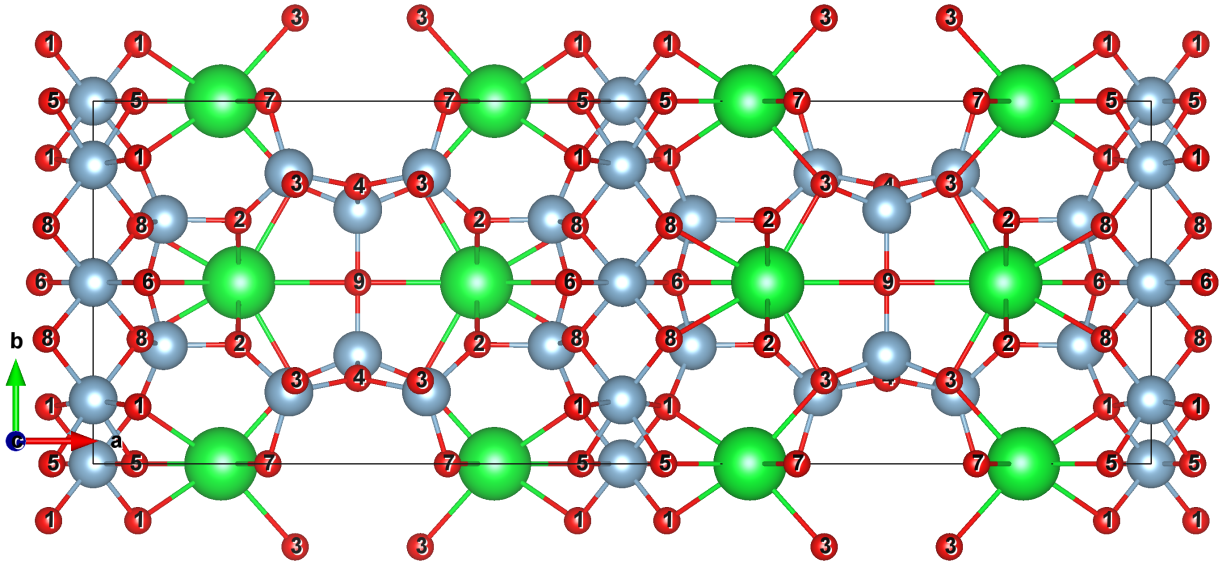

Fig. S3 Symmetrically non-equivalent O sites. Strontium, aluminium and oxygen atoms are represented by green, blue and red spheres, respectively.

IV pDOS of symmetrically non-equivalent site

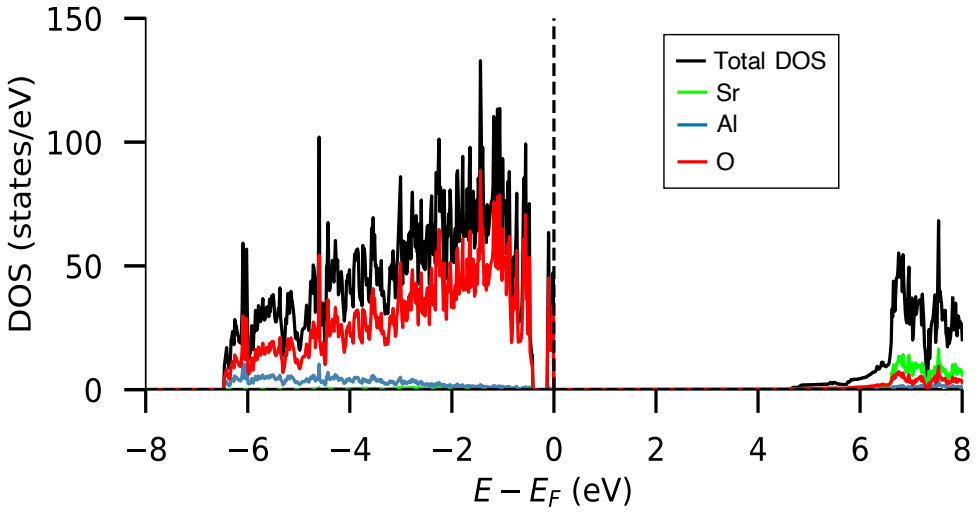

Fig. S4 pDOS of atomic species.

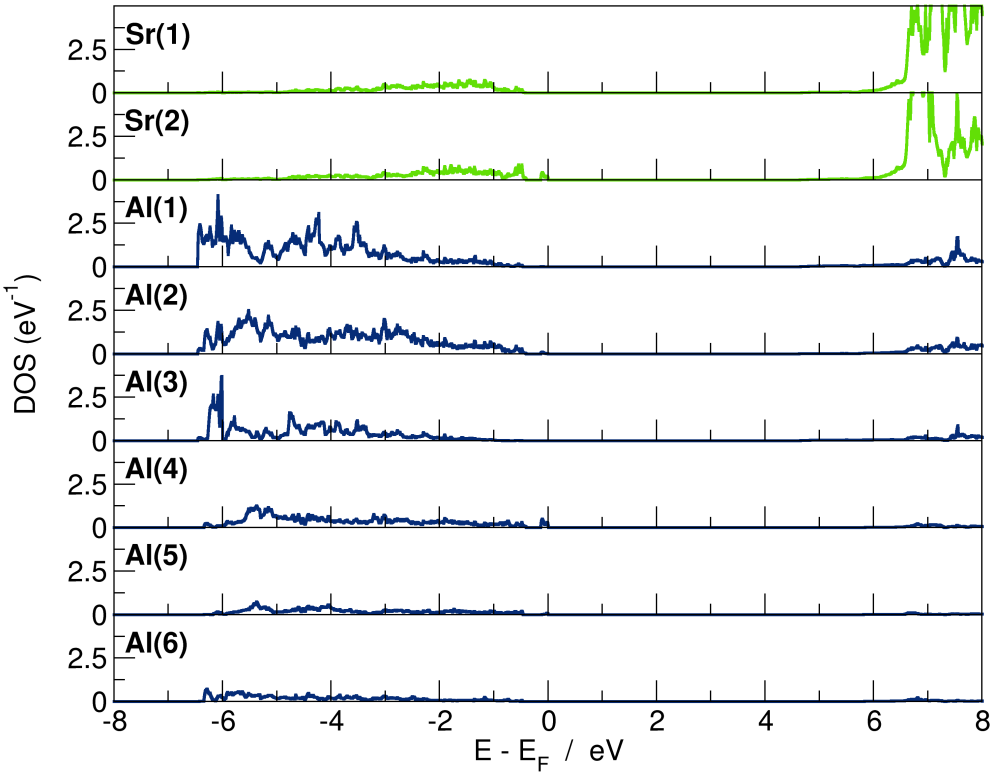

Fig. S5 pDOS of symmetrically non-equivalent Sr and Al sites.

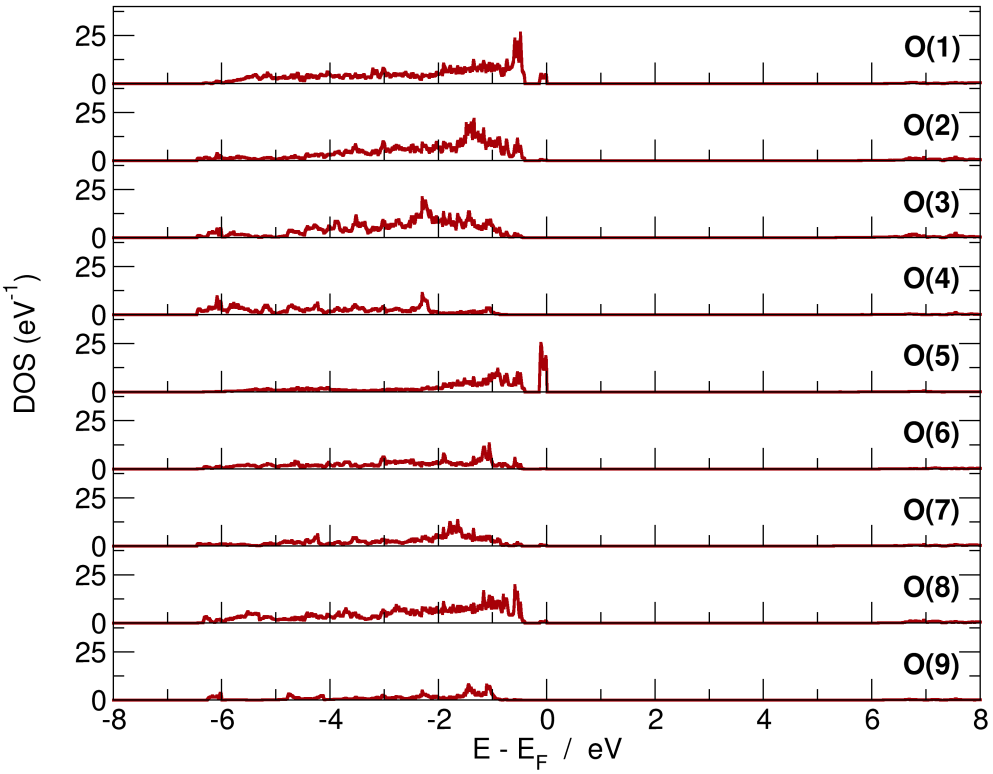

Fig. S6 pDOS of symmetrically non-equivalent O sites.

V Charge density at the top of the valence band

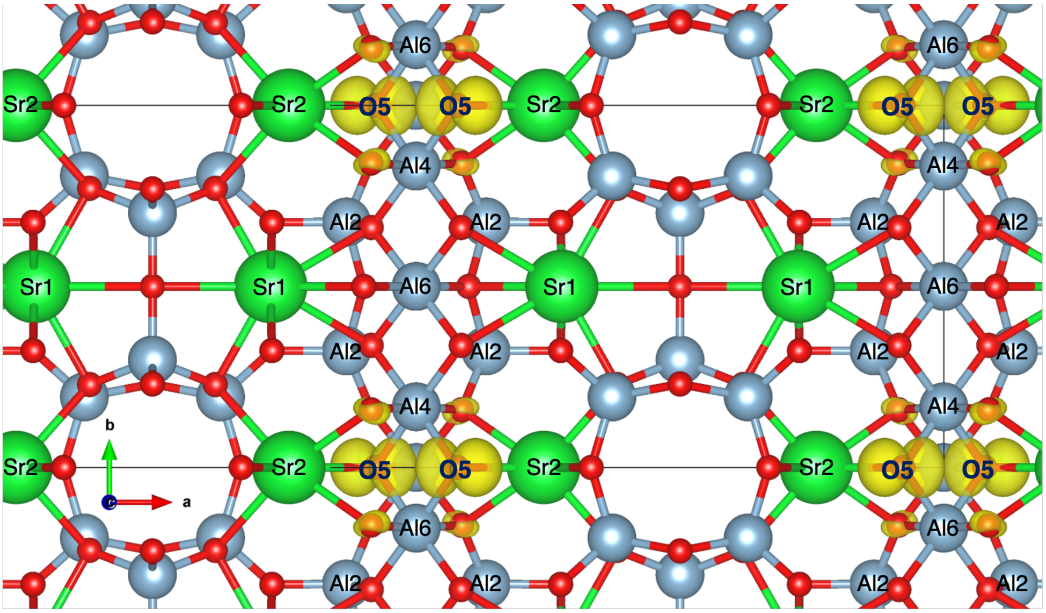

Fig. S7 Charge density associated to the top of the valence band (isovalue level = 0.01 e/a_0^3).

VI Interstitial point defects

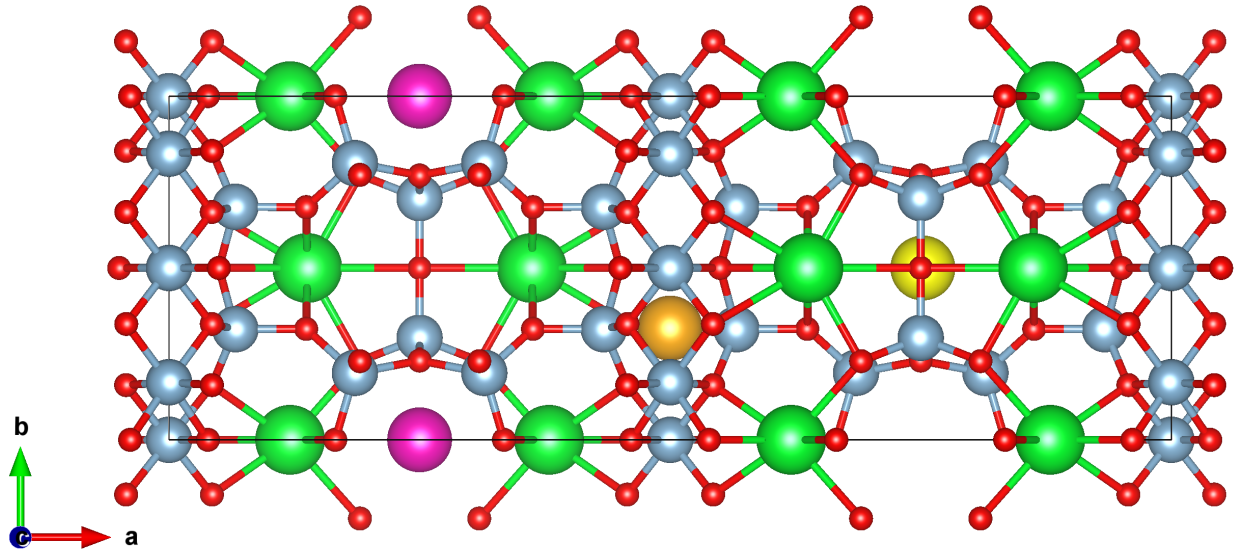

Fig. S8 Initial positions of interstitial point defects within the $Sr_4Al_{14}O_{25}$ structure. Sr, Al and O atoms are represented by green, blue and red spheres, respectively. For a general defect D, the initial positions of interstitials within the supercell are shown by i) pink sphere for $D_{i(1)}$ = (x=0.25, y=0.00, z=0.80), ii) yellow sphere for $D_{i(2)}$ = (x=0.75, y=0.50, z=0.68), and iii) orange sphere for $D_{i(3)}$ = (x=0.50, y=0.325, z=0.25).

VII Defect formation enthalpies

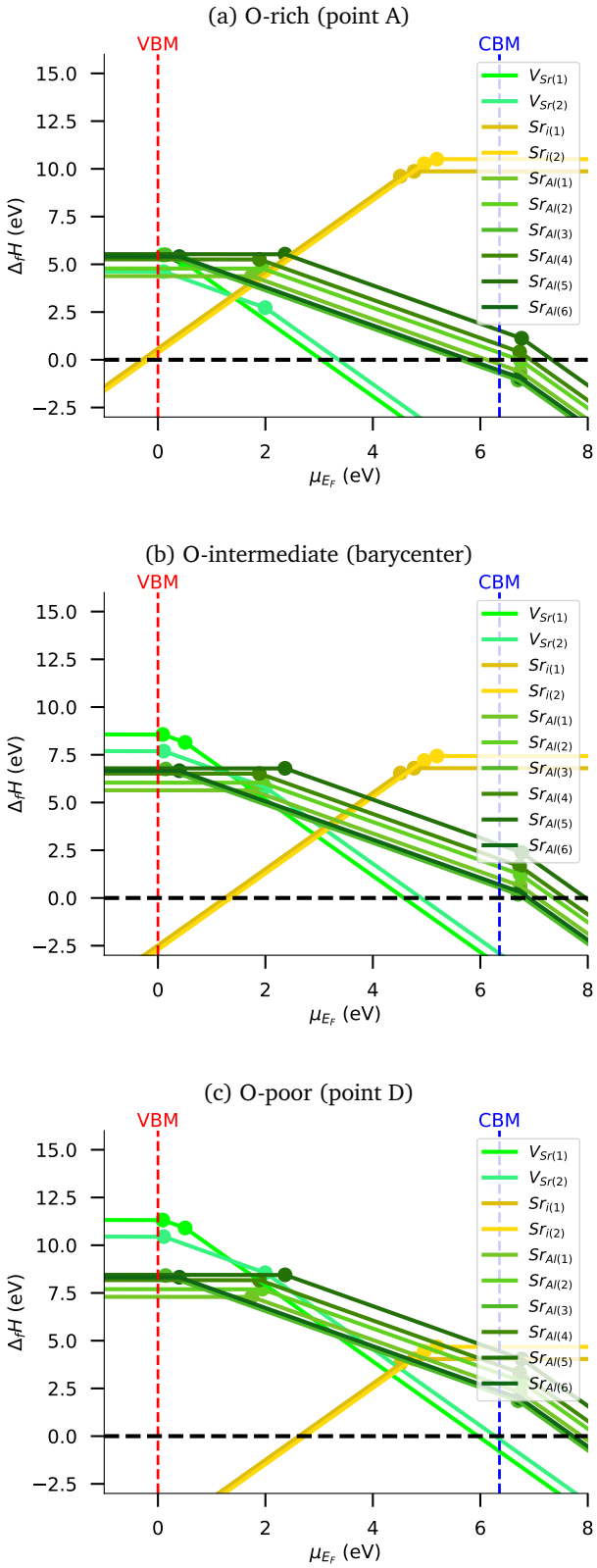

Fig. S9 Defect formation enthalpies *vs* μ_{E_F} for Sr point defects under a) O-rich, b) O-intermediate and c) O-poor atmospheres.

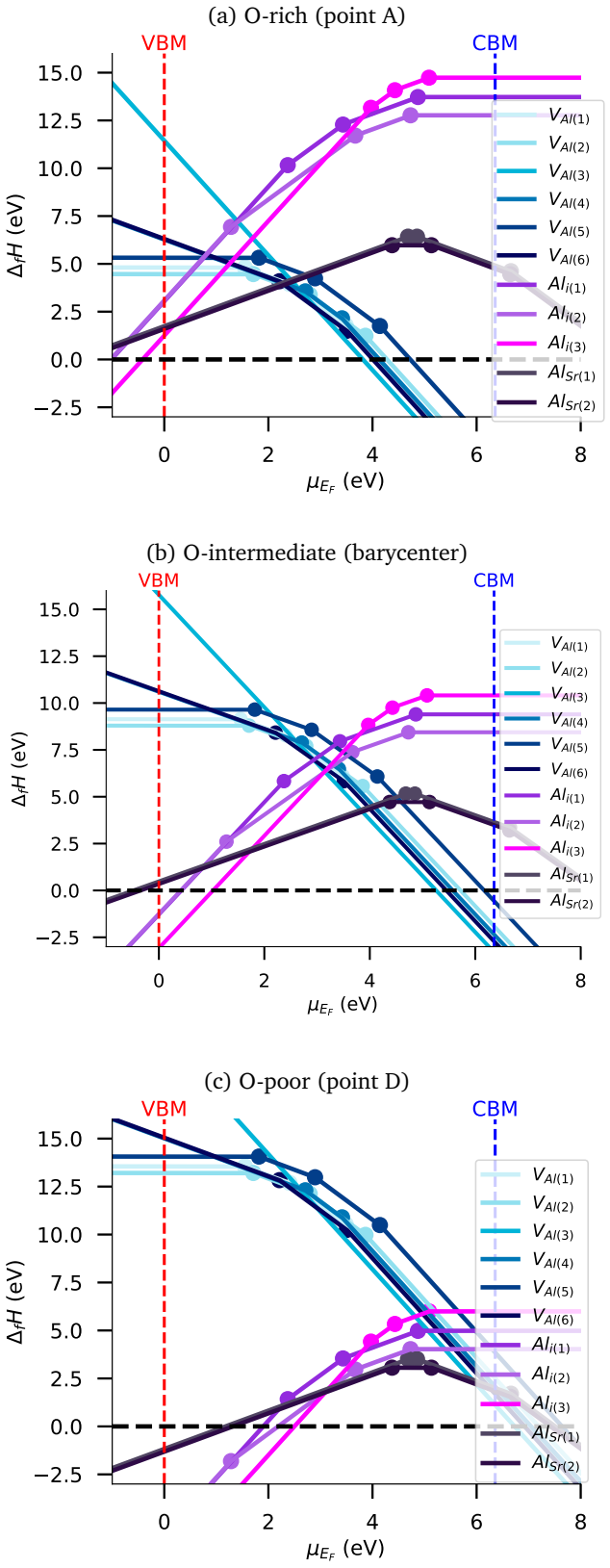

Fig. S10 Defect formation enthalpies *vs* μ_{E_F} for Al point defects under a) O-rich, b) O-intermediate and c) O-poor atmospheres.

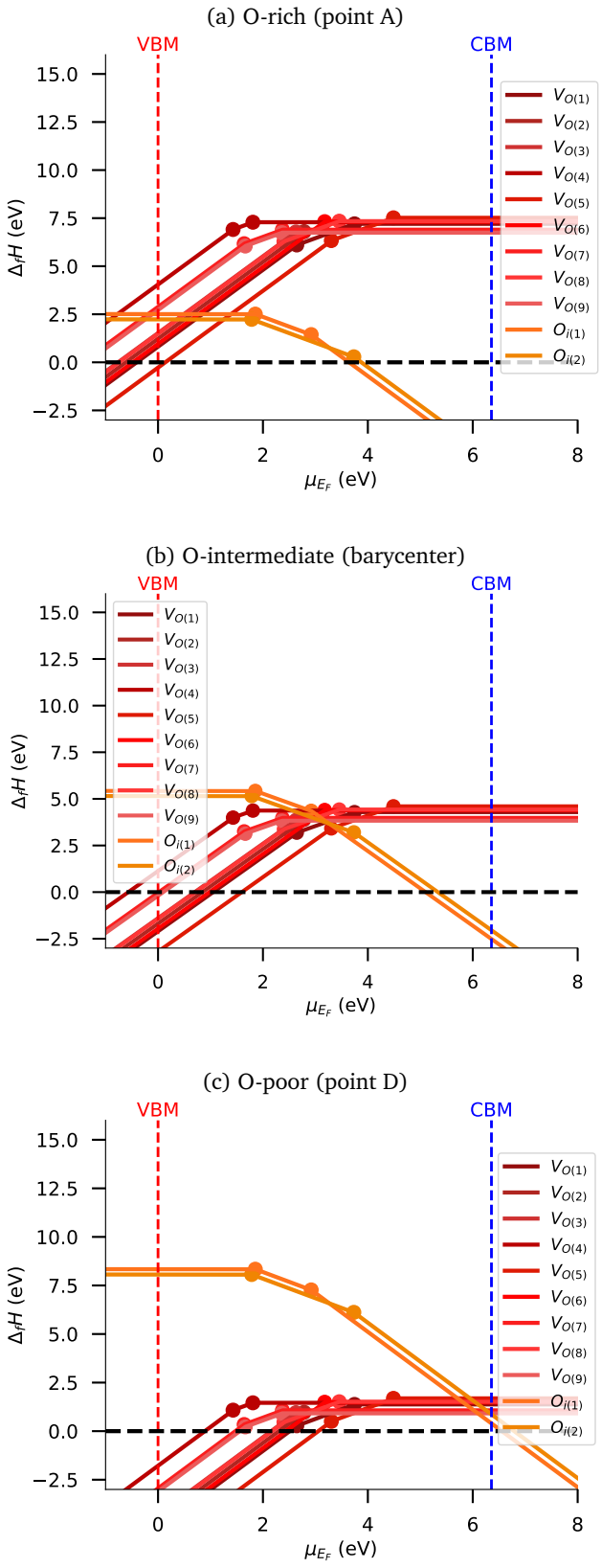

Fig. S11 Defect formation enthalpies *vs* μ_{E_F} for O point defects under a) O-rich, b) O-intermediate and c) O-poor atmospheres.

VIII pDOS of a representative set of point defects

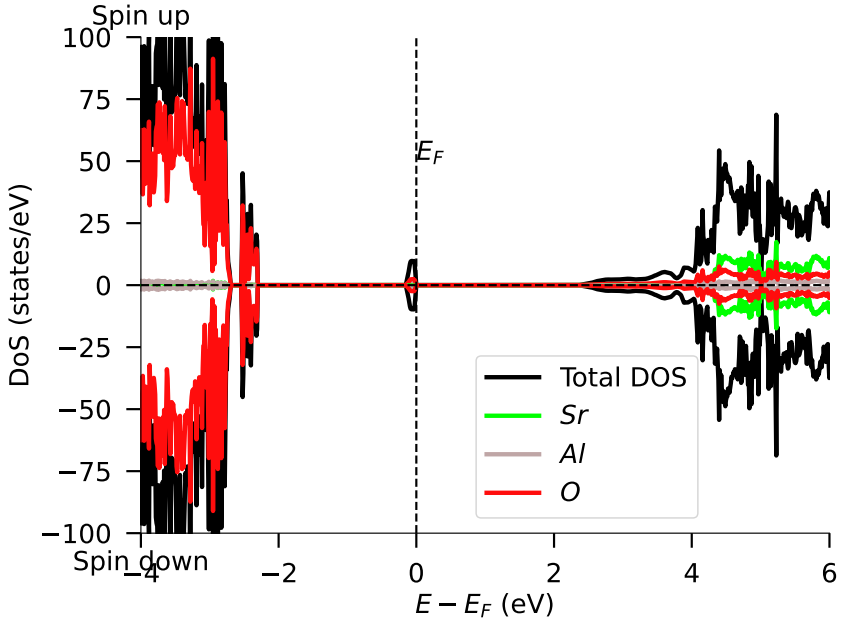

Fig. S12 pDOS of oxygen vacancy $V^0_{O(1)}$.

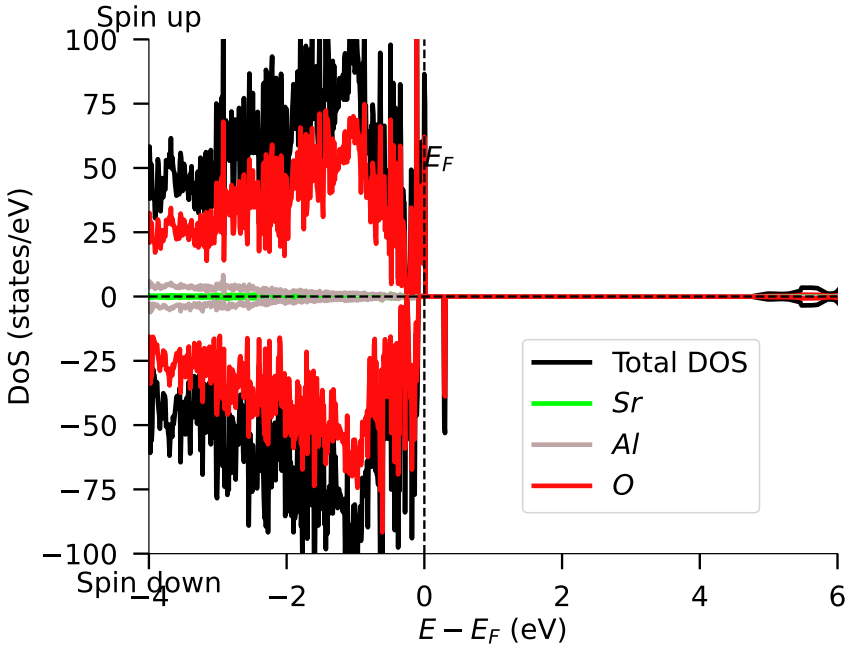

Fig. S13 pDOS of strontium vacancy $V^0_{Sr(2)}$.

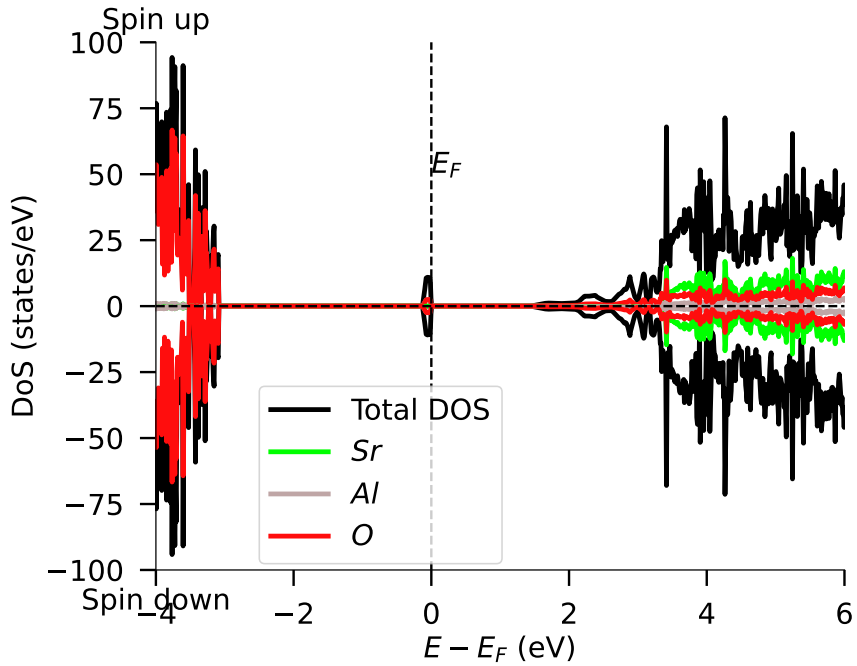

Fig. S14 pDOS of aluminium substituting strontium $Al^{-1}_{Sr(1)}$.

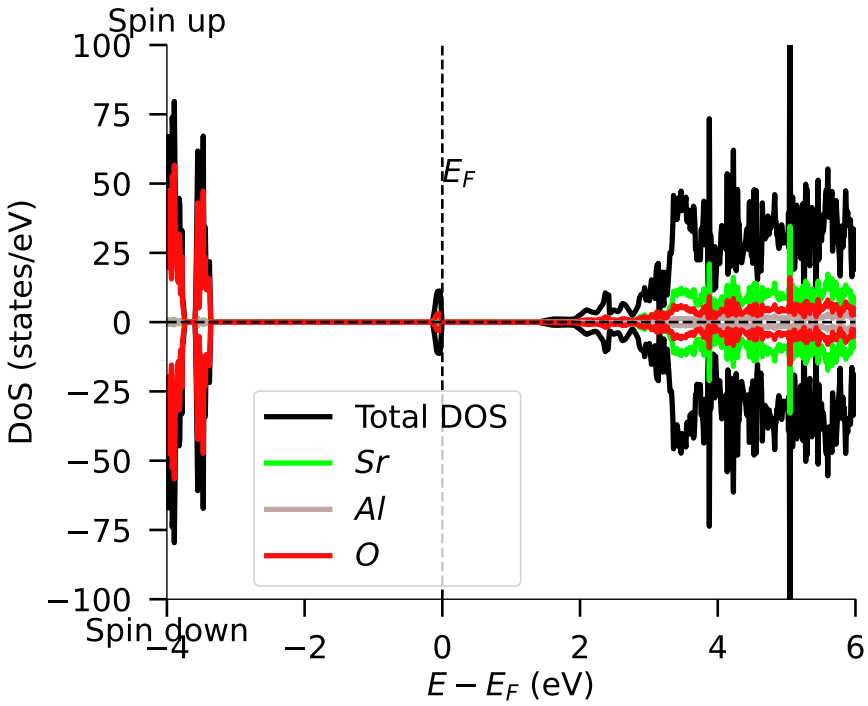

Fig. S15 pDOS of strontium interstitial $Sr^{0}_{i(1)}$.

IX Charge transition levels

Defect	q/q'	$\varepsilon(q/q')$
$V_{Sr(1)}$	0/-1	0.09 eV
$V_{Sr(1)}$	-1/-2	0.51 eV
$V_{Sr(2)}$	0/-1	0.11 eV
$V_{Sr(2)}$	-1/-2	2.00 eV
$Sr_{i(1)}$	+2/+1	4.51 eV
$Sr_{i(1)}$	+1/0	4.77 eV
$Sr_{i(2)}$	+2/+1	4.96 eV
$Sr_{i(2)}$	+1/0	5.19 eV
$Sr_{Al(1)}$	0/-1	1.74 eV
$Sr_{Al(1)}$	-1/-2	6.74 eV
$Sr_{Al(2)}$	0/-1	1.95 eV
$Sr_{Al(2)}$	-1/-2	6.75 eV
$Sr_{Al(3)}$	0/-1	0.14 eV
$Sr_{Al(3)}$	-1/-2	6.70 eV
$Sr_{Al(4)}$	0/-1	1.89 eV
$Sr_{Al(4)}$	-1/-2	6.73 eV
$Sr_{Al(5)}$	0/-1	2.37 eV
$Sr_{Al(5)}$	-1/-2	6.77 eV
$Sr_{Al(6)}$	0/-1	0.40 eV
$Sr_{Al(6)}$	-1/-2	6.75 eV

Table S2 Charge transition levels of Sr-based defect species.

Defect	q/q'	$\varepsilon(q/q')$
$V_{Al(1)}$	0/-1	1.55 eV
$V_{Al(1)}$	-1/-2	2.41 eV
$V_{Al(1)}$	-2/-3	3.49 eV
$V_{Al(2)}$	0/-1	1.71 eV
$V_{Al(2)}$	-1/-2	2.79 eV
$V_{Al(2)}$	-2/-3	3.87 eV
$V_{Al(4)}$	0/-1	-1.88 eV
$V_{Al(4)}$	-1/-2	2.71 eV
$V_{Al(4)}$	-2/-3	3.42 eV
$V_{Al(5)}$	0/-1	1.82 eV
$V_{Al(5)}$	-1/-2	2.90 eV
$V_{Al(5)}$	-2/-3	4.14 eV
$V_{Al(6)}$	0/-1	-2.21 eV
$V_{Al(6)}$	-1/-2	2.21 eV
$V_{Al(6)}$	-2/-3	3.51 eV
$Al_{i(1)}$	+3/+2	2.37 eV
$Al_{i(1)}$	+2/+1	3.43 eV
$Al_{i(1)}$	+1/0	4.88 eV
$Al_{i(2)}$	+3/+2	1.28 eV
$Al_{i(2)}$	+2/+1	3.67 eV
$Al_{i(2)}$	+1/0	4.73 eV
$Al_{i(3)}$	+3/+2	3.97 eV
$Al_{i(3)}$	+2/+1	4.43 eV
$Al_{i(3)}$	+1/0	5.09 eV
$Al_{Sr(1)}$	+1/0	4.68 eV
$Al_{Sr(1)}$	0/-1	4.86 eV
$Al_{Sr(1)}$	-1/-2	6.66 eV
$Al_{Sr(2)}$	+1/0	4.38 eV
$Al_{Sr(2)}$	0/-1	5.13 eV
$Al_{Sr(2)}$	-1/-2	6.65 eV

Table S3 Charge transition levels of Al-based defect species.

Defect	q/q'	$\varepsilon(q/q')$
$V_{O(1)}$	+2/+1	2.65 eV
$V_{O(1)}$	+1/0	3.75 eV
$V_{O(2)}$	+2/0	2.79 eV
$V_{O(3)}$	+2/0	2.63 eV
$V_{O(4)}$	+2/+1	1.43 eV
$V_{O(4)}$	+1/0	1.81 eV
$V_{O(5)}$	+2/+1	3.30 eV
$V_{O(5)}$	+1/0	4.49 eV
$V_{O(6)}$	+2/0	3.18 eV
$V_{O(7)}$	+2/+1	1.64 eV
$V_{O(7)}$	+1/0	2.37 eV
$V_{O(8)}$	+2/+1	2.40 eV
$V_{O(8)}$	+1/0	3.46 eV
$V_{O(9)}$	+2/+1	1.66 eV
$V_{O(9)}$	+1/0	2.36 eV
$O_{i(1)}$	0/-1	1.86 eV
$O_{i(1)}$	-1/-2	2.92 eV
$O_{i(2)}$	0/-1	1.76 eV
$O_{i(2)}$	-1/-2	3.73 eV

Table S4 Charge transition levels of O-based defect species.

X Defect concentrations

a) O-rich (point A)

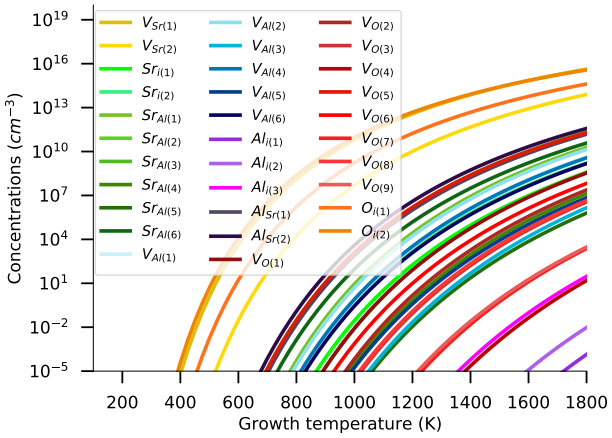

(b) O-intermediate (barycenter)

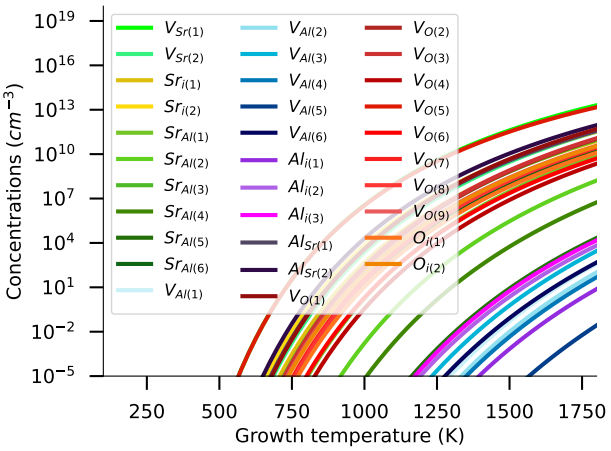

(c) O-poor (point D)

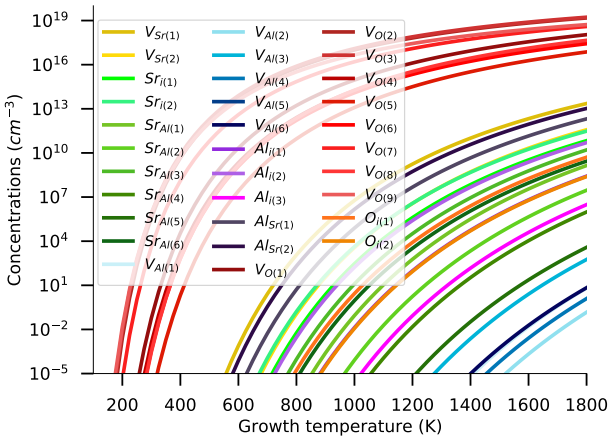

Fig. S16 Defect concentrations *vs* the growth temperature T_{gr} under a) O-rich, b) O-intermediate and c) O-poor atmospheres.

Defect	O-rich	O-intermediate	O-poor
$Sr_{i(1)}$	9.86×10^{6}	4.06×10^{9}	3.35×10^{9}
$Sr_{i(2)}$	5.27×10^{7}	2.17×10^{10}	1.79×10^{10}
$V_{Sr(1)}$	7.22×10^{14}	1.75×10^{12}	2.13×10^{12}
$V_{Sr(2)}$	8.32×10^{12}	1.73×10^{10}	2.10×10^{10}
$Sr_{Al(1)}$	6.54×10^{8}	2.43×10^{8}	3.55×10^{7}
$Sr_{Al(2)}$	8.36×10^{6}	3.11×10^{6}	4.53×10^{5}
$Sr_{Al(3)}$	1.11×10^{10}	4.15×10^{9}	6.04×10^{8}
$Sr_{Al(4)}$	1.99×10^{5}	7.40×10^{4}	1.08×10^{4}
$Sr_{Al(5)}$	7.25×10^{3}	1.60×10^{2}	2.33×10^{1}
$Sr_{Al(6)}$	1.68×10^{9}	6.26×10^{8}	9.12×10^{7}
$V_{Al(1)}$	1.23×10^{8}	1.45	1.50×10^{-2}
$V_{Al(2)}$	4.55×10^{8}	3.19×10^{-1}	2.13×10^{-4}
$V_{Al(3)}$	1.57×10^{4}	1.42×10^{1}	2.51
$V_{Al(4)}$	1.13×10^{8}	1.46×10^{-1}	2.57×10^{-3}
$V_{Al(5)}$	1.05×10^{5}	3.50×10^{-5}	3.12×10^{-9}
$V_{Al(6)}$	4.47×10^{7}	2.13	1.90×10^{-2}
$Al_{Sr(1)}$	7.73×10^{9}	2.08×10^{10}	1.43×10^{11}
$Al_{Sr(2)}$	2.16×10^{10}	5.80×10^{10}	8.93×10^{11}
$Al_{i(1)}$	1.07×10^{-7}	2.26×10^{-2}	6.49×10^{6}
$Al_{i(2)}$	1.22×10^{-5}	4.58×10^{1}	2.37×10^{9}
$Al_{i(3)}$	9.75×10^{-2}	1.08×10^{2}	3.94×10^{4}
$V_{O(1)}$	7.64×10^{6}	2.68×10^{10}	3.61×10^{17}
$V_{O(2)}$	3.80×10^{5}	4.58×10^{9}	6.85×10^{18}
$V_{O(3)}$	4.55×10^{4}	5.24×10^{9}	7.84×10^{18}
$V_{O(4)}$	4.33×10^{-2}	6.63×10^{7}	9.91×10^{16}
$V_{O(5)}$	1.04×10^{10}	1.37×10^{12}	1.89×10^{16}
$V_{O(6)}$	1.32×10^{6}	1.75×10^{8}	7.99×10^{16}
$V_{O(7)}$	1.28×10^{1}	1.11×10^{9}	1.66×10^{18}
$V_{O(8)}$	5.85×10^{4}	1.20×10^{9}	1.33×10^{17}
$V_{O(9)}$	1.81×10^{1}	1.69×10^{9}	2.52×10^{18}
$O_{i(1)}$	5.83×10^{13}	4.64×10^{8}	1.81×10^{8}
$O_{i(2)}$	7.01×10^{14}	1.56×10^{9}	5.99×10^{6}

Table S5 Defect concentrations under different synthesis conditions at T_{gr} = 1600 K.

Notes and references

1 E. Péan, J. Vidal, S. Jobic and C. Latouche, *Chemical Physics Letters*, 2017, **671**, 124–130.

2 A. Stoliaroff, S. Jobic and C. Latouche, *Journal of Computational Chemistry*, 2018, **39**, 2251–2261.

3 D. Dutczak, T. Jüstel, C. Ronda and A. Meijerink, *Physical Chemistry Chemical Physics*, 2015, **17**, 15236–15249.

4 E. Burstein, *Physical Review*, 1954, **93**, 632–633.

5 T. S. Moss, *Proceedings of the Physical Society. Section B*, 1954, **67**, 775–782.

6 S. Lany and A. Zunger, *Modelling and Simulation in Materials Science and Engineering*, 2009, **17**, 084002.